Acoustic Metamaterials with Independently Tunable Mass, Damping, and Stiffness

Vinod Ramakrishnan and Michael J. Frazier[a)]
Department of Mechanical and Aerospace Engineering, University of California, San Diego, California 92093, USA

(Dated: 19 April 2022)

We report on a class of acoustic metamaterial lattices which exploit multi-stability and kinematic amplification to independently adjust the local effective mass, damping, and stiffness properties, thereby realizing congruent alterations to the dispersion response post-fabrication. The fundamental structural tuning element permits a broad range in the effective property space; moreover, its particular design carries the benefit of tuning without altering the original size/shape of the emerging metamaterial structure. The relation between the tuning element geometry and the achieved variability in effective properties is explored. Bloch's theorem facilitates the dynamic analysis of representative 1D/2D systems, revealing, e.g., band-gap formation/closure/migration and positive/negative metadamping in accordance with the tuning element configuration. To demonstrate a utility, we improvise a waveguide by appropriately patterning the tuning element configuration within 2D system. We believe that the proposed strategy offers a new way to expand the range of performance and functionality of metamaterial lattices.

I. INTRODUCTION

Architected materials are a type of engineered media characterized by an internal structure which engenders extraordinary effective properties and functionalities, and thus, have stimulated research across the range of materials science and engineering, including the thermal[1,2], optical[3,4], acoustic[5–7], mechanical[8–10], and biological[11,12] sectors. In the context of elastodynamics, architected materials (i.e., phononic materials[13]) utilize the internal structure to manipulate the scattering and resonance phenomena peculiar to wave propagation, enabling an engineered dynamic response that has realized, e.g., negative[14–16], amplified[17,18], and (analogous) quantum mechanical[19–22] properties, and provided a foundation for new and expanded functionalities[23] and applications[24]. The periodicity of typical phononic material architectures mimics that of crystalline solids; although, where the fundamental repeating element (i.e., unit cell) which shapes the overall material response is a "structural molecule" of custom geometry and composition. On a parallel track, advancements in 3D-printing technology enable the physical realization of increasingly complex unit cell designs at progressively smaller scales, allowing evermore precise tailoring of the corresponding dynamic response. However, once fabricated, the unit cell architecture is, generally, static and, thus, the resulting phononic material is ill-suited for applications with changing operational requirements. To broaden the range of response and enhance the functionality of phononic materials, a tuning capacity instituted at the architectural level is desirable and the overall aim of this article.

[a)]Corresponding author email: mjfrazier@ucsd.edu

On the matter of tuning phononic material performance post-fabrication, several strategies are summarized in the literature, including mechanical pre-loading[25–27], integrated piezoelectric[28–33] and electromagnetic[34,35] elements, phase transitions[36,37], mass redistribution[38–40], and geometric instability[41–44]. In general, the tuning is continuous, granting smooth adjustments to performance; moreover, it is facilitated via reversible processes, granting repeatability. However, while these diverse approaches are able to manipulate the effective mass, damping, and stiffness that govern the observed dynamic response, typically, the achieved tuning capability is limited to a single material property; still, methods that couple two or more properties tacitly accept trade-off and compromise in their manipulation. For greater control of the wave dynamics, the literature is wanting in a strategy that independently tunes all three properties which this article aims to address, specifically.

In addition to the above-listed techniques, geometric multi-stability[45–50] has also been exploited as a tuning mechanism; although, one which demands neither specific material constituents nor constant stimulation in regard to implementation within the architecture and activation/stabilization of the tuned state. Utilizing this approach, mechanically switching the architecture to any of several discrete configurations realizes a unique effective stiffness, often accompanied by a residual strain. Recently, Frazier[51] combined multi-stability and kinematic amplification to tune the effective mass without material transport or residual strain. Utilizing this design a template, this article proposes a tuning element which effects additional tuning capabilities in the stiffness and damping parameters in order to complete the property triad. We demonstrate the design strategy in one- and two-dimensional lattices where the specific configuration of the tuning element is reflected in the distinct frequency and damping ratio band diagrams

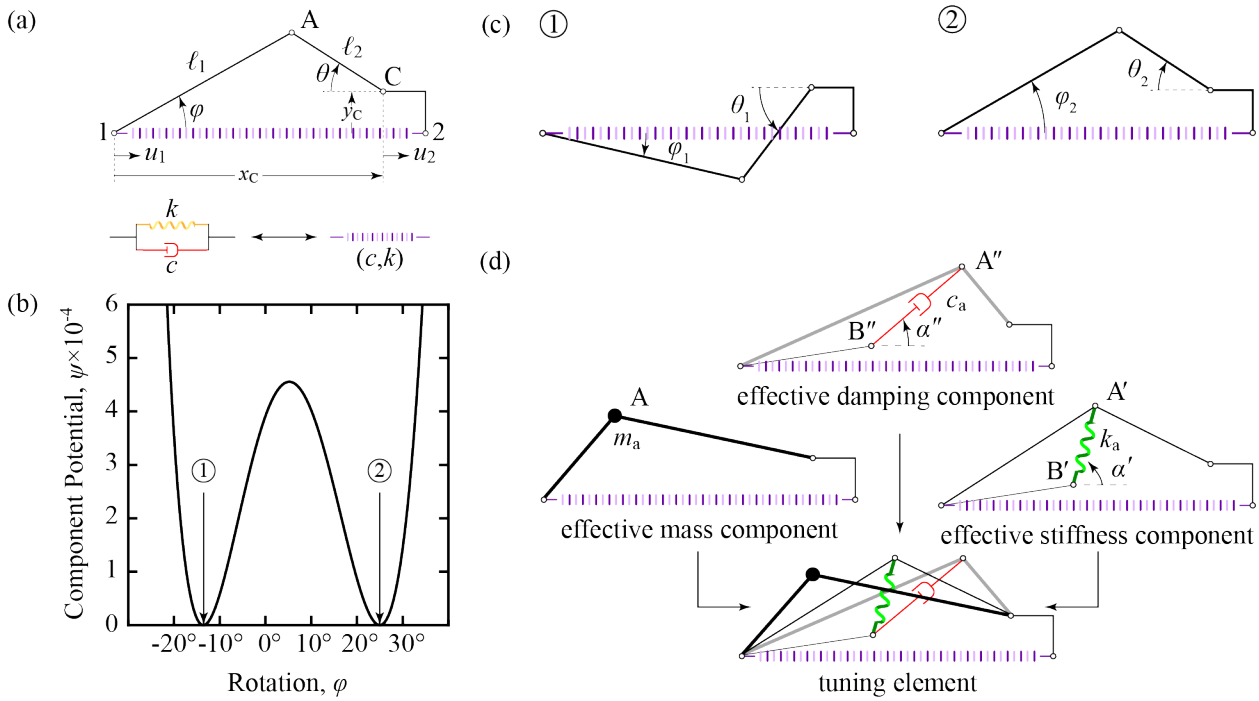

FIG. 1. Multi-stable Tuning Element. (a) The bi-stable kinematic amplification component including two-bar linkage and offset. (b) The potential energy landscape indicating the component bi-stability and, by virtue of the symmetry, the recoverability of the elastic components. (c) Stable configurations, labeled according to φ_s where $\varphi_1 < \varphi_2$. (d) The mass, damping, and stiffness components forming the tuning element.

produced by the associated complex dispersion relations with variable material coefficients. In re-configuring the tuning element, we observe the formation, closure, and migration of band gaps, a change in the sonic wave speed, and both positive and negative metadamping. As an exemplary application, we construct a waveguide within a 2D system by spatially prescribing the effective property-linked element configuration, demonstrating a post-fabrication custom morphology in support of a desired function.

II. MODEL DESCRIPTION

A. The Multi-stable Element

Central to the metamaterial tuning ability are the multi-stability and kinematic amplification provided by the internal architecture. To realize these effects, we exploit the geometry proposed by Frazier[51] (Fig. 1a) as a key component of the tuning element that, ultimately, enables adjustments to the effective properties. The component comprises a simple, two-bar linkage together with a linear spring of stiffness, k, and a fluid damper of viscosity, c, coupling the motion of the free ends, i.e., nodes 1 and C. As the spring penalizes deformation, the component possesses a finite number of energetically stable arrangements distinguished by the configuration parameter, $\varphi \in [-\pi, \pi]$. Written explicitly, the configuration-dependent deformation energy is expressed as follows:

$$\psi(\varphi) = \frac{k}{2}\left(\sqrt{\ell_2^2 - [y_C - \ell_1\sin(\varphi)]^2} - |x_C - \ell_1\cos(\varphi)|\right)^2. \tag{1}$$

For a particular set of material and geometric parameters, Fig. 1b depicts the energy landscape described by Eq. (1), revealing two degenerate minimum-energy states, φ_s, $s = 1, 2$ (Fig. 1c) indicative of both the component bi-stability and recoverability, i.e., the component length regains its undeformed value within each stable configuration. In addition, within the component, we identify two axes of deformation: the primary axis extending through nodes 1 and 2, and the secondary axis passing through nodes 1 and C. Since the two axes are non-parallel, $\varphi_1 \neq \varphi_2$ such that the response at node A is configuration-specific. Through the rigid links, the motion of node A is directly related to that of the free ends. For small amplitude displacements along the primary axis (see Appendix):

$$u_A = \frac{u_2 + \tan(\theta_s)\cot(\varphi_s)u_1}{1 + \tan(\theta_s)\cot(\varphi_s)}, \tag{2a}$$

$$v_A = (u_1 - u_2)\frac{\cos(\varphi_s)\cos(\theta_s)}{\sin(\varphi_s + \theta_s)}. \tag{2b}$$

The multi-stable tuning element (Fig. 1d) assembles three of the above-described components in order

to effect independent adjustments to the effective mass, stiffness, and damping. For clarity, equivalent parameters in the mass, stiffness, and damping components are bare, primed, and double-primed, respectively. Apparently, the inertia supplied by mass, m_a, resists the acceleration of node A. Similarly, k_a opposes the relative displacement between nodes A$'$ and B$'$; c_a opposes the relative velocity between nodes A$''$ and B$''$. To ensure that the deformation energy vanishes in each of the stable configurations (i.e., the element regains its undeformed length), we place node B$'$ along the secondary axis. To simplify the subsequent presentation, B$''$ is assumed co-located with B$'$. Through rigid connections, the motions of nodes B$'$ and C mirror those of nodes 1 and 2, respectively.

In general, for a tuning element comprising n components, there are as many as 2^n stable configurations (Fig. S1a). In order to effect a transition between all possible configurations, care is taken to ensure that the two-bar linkages within a tuning element attain their maximum extension simultaneously (Mov. S1). To this end, for simplicity, the present construction utilizes linkages with identical extended length, but variable lengths for the constituent bars. In addition, each linkage connects to the same nodes (e.g., nodes 1 and C). Essentially, linkages are constructed following an ellipse: linkages connect nodes 1 and C (i.e., the focii) and have an extended length that is twice the semi-major axis; internal joints A, A$'$, and A$''$ lie along the ellipse perimeter.

B. Effective Properties

To characterize the performance of the tuning element, we consider the dynamics of the isolated unit cell in Fig. 1e. The relevant equations of motion emerge from the dissipative Euler-Lagrange equation, $(\mathcal{L}_{,\dot{\mathbf{u}}})_{,t} - \mathcal{L}_{,\mathbf{u}} + R_{,\dot{\mathbf{u}}} = \mathbf{0}$, with Lagrangian, $\mathcal{L}(\mathbf{u}, \dot{\mathbf{u}})$, and viscous dissipation function, $R(\dot{\mathbf{u}})$. We define the dimensionless displacement and time variables, $\bar{u} = u/a$ and $\bar{t} = \omega_0 t$ where $\omega_0 = \sqrt{k/m}$. Utilizing these definitions and dividing by ka^2, the corresponding non-dimensional kinetic energy, T, deformation energy, V, and rate of energy loss, R, are expressed as follows:

$$T = \frac{1}{2}\dot{\bar{u}}_1^2 + \frac{1}{2}\bar{m}_\mathrm{a}\dot{\bar{u}}_\mathrm{A}^2 + \frac{1}{2}\bar{m}_\mathrm{a}\dot{\bar{v}}_\mathrm{A}^2, \tag{3a}$$

$$V = \frac{1}{2}(\bar{u}_2 - \bar{u}_1)^2 + \frac{1}{2}\bar{k}_\mathrm{a}(\delta\bar{\ell}_\mathrm{AB})^2, \tag{3b}$$

$$R = \frac{1}{2}\bar{c}(\dot{\bar{u}}_2 - \dot{\bar{u}}_1)^2 + \frac{1}{2}\bar{c}_\mathrm{a}(\delta\dot{\bar{\ell}}_\mathrm{AB})^2, \tag{3c}$$

where $\bar{m}_\mathrm{a} = m_\mathrm{a}/m$, $\bar{k}_\mathrm{a} = k_\mathrm{a}/k$, $\bar{c} = c/m$, and $\bar{c}_\mathrm{a} = c_\mathrm{a}/m$ denote the normalized material parameters; $\delta\bar{\ell}_\mathrm{AB}$ is the change in the length of the line joining nodes A$'$ (or A$''$) and B$'$.

Substituting the definitions from Eq. (2) into Eq. (3), $\mathcal{L}(\mathbf{u}, \dot{\mathbf{u}})$ and $R(\dot{\mathbf{u}})$ become sole functions of the time-dependent boundary displacements $\mathbf{u}^\mathrm{T} = [u_1 \; u_2]$. The dissipative Euler-Lagrange's equation yields the unit cell matrix equations of motion, $\mathbf{M}\ddot{\bar{\mathbf{u}}} + \mathbf{C}\dot{\bar{\mathbf{u}}} + \mathbf{K}\bar{\mathbf{u}} = \mathbf{0}$, where

$$\mathbf{M} = \begin{bmatrix} 1 + \bar{m}_\mathrm{a}\delta_{11} & -\bar{m}_\mathrm{a}\delta_{12}/2 \\ -\bar{m}_\mathrm{a}\delta_{21}/2 & \bar{m}_\mathrm{a}\delta_{22} \end{bmatrix}, \tag{4a}$$

$$\mathbf{C} = (\bar{c} + \bar{c}_\mathrm{a}\varepsilon_\mathrm{c}) \begin{bmatrix} 1 & -1 \\ -1 & 1 \end{bmatrix}, \tag{4b}$$

$$\mathbf{K} = (1 + \bar{k}_\mathrm{a}\varepsilon_\mathrm{k}) \begin{bmatrix} 1 & -1 \\ -1 & 1 \end{bmatrix}, \tag{4c}$$

are the tunable mass, damping, and stiffness matrices, respectively; δ_{ij}, ε_c, and ε_k are configuration-dependent tuning coefficients:

$$\delta_{11} = \left[\cos(\varphi_s)\csc(\varphi_s + \theta_s)\right]^2,$$
$$\delta_{12} = \delta_{21} = 2\cos(\varphi_s)\cos(\theta_s)\csc(\varphi_s + \theta_s)\cot(\varphi_s + \theta_s),$$
$$\delta_{22} = \left[\cos(\theta_s)\csc(\varphi_s + \theta_s)\right]^2,$$
$$\varepsilon_\mathrm{c} = \left[\frac{\cos(\alpha_s'') - \sin(\alpha_s'')\cot(\varphi_\mathrm{s}'')}{1 + \cot(\varphi_\mathrm{s}'')\tan(\theta_\mathrm{s}'')}\right]^2,$$
$$\varepsilon_\mathrm{k} = \left[\frac{\cos(\alpha_s') - \sin(\alpha_s')\cot(\varphi_\mathrm{s}')}{1 + \cot(\varphi_\mathrm{s}')\tan(\theta_\mathrm{s}')}\right]^2.$$

Recognizing that the isolated unit cell possesses only a single non-zero mode of vibration reduces the governing equations to $m_\mathrm{eff}\ddot{\bar{u}} + 4c_\mathrm{eff}\dot{\bar{u}} + 4k_\mathrm{eff}\bar{u} = 0$, where

$$m_\mathrm{eff} = 1 + \bar{m}_\mathrm{a}(\delta_{11} + \delta_{22} + \delta_{12}), \tag{5a}$$

$$c_\mathrm{eff} = \bar{c} + \bar{c}_\mathrm{a}\varepsilon_\mathrm{c}, \tag{5b}$$

$$k_\mathrm{eff} = 1 + \bar{k}_\mathrm{a}\varepsilon_\mathrm{k}, \tag{5c}$$

denote the configuration-dependent element effective mass, damping, and stiffness. Thus, integrated within internal architectures, the multi-stable tuning element presents the opportunity to tailor acoustic metamaterial dynamic performance post-fabrication via geometric re-configuration, i.e., without the need to add/remove material or to invoke stimuli-response constituents.

As an illustration of the potential disparity in effective properties exhibited by the element's bi-stable components, Fig. 2 plots the effective property ratios, $m_\mathrm{r} = m_\mathrm{eff}^{(1)}/m_\mathrm{eff}^{(2)}$, $c_\mathrm{r} = c_\mathrm{eff}^{(1)}/c_\mathrm{eff}^{(2)}$, and $k_\mathrm{r} = k_\mathrm{eff}^{(1)}/k_\mathrm{eff}^{(2)}$ (superscript denoting the configuration, s, of the respective component) as functions of the geometric design parameters for $\bar{m}_\mathrm{a} = 1/10$, $\bar{k}_\mathrm{a} = 4$, $\bar{c}_\mathrm{a} = 3/2$, and $\bar{c} = 1/2$. In Fig. 2a, effective property curves are generated by considering the component response when the internal joint (i.e., A, A$'$, or A$''$) is positioned at an arbitrary location (as defined by φ_s, φ_s', or φ_s'') along the ellipse. The m_r approaches a maximum as $\varphi_1 \to 0$ ($\varphi_2 \to \pi/2$) where the inertial amplification effect generated by the effective mass component is at a peak (nadir). Specifically, for a static mass, $m_\mathrm{st} = 1 + \bar{m}_\mathrm{a}$, the maximum corresponds to $m_\mathrm{eff}^{(1)}/m_\mathrm{st} = 5.67$ and $m_\mathrm{eff}^{(2)}/m_\mathrm{st} = 1.32$, indicating a less inconsequential

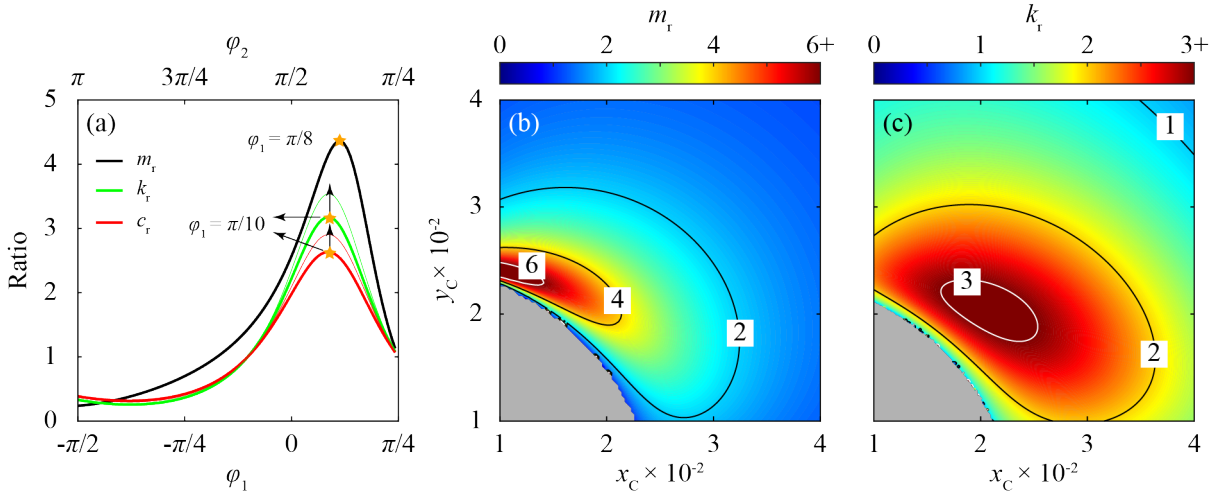

FIG. 2. Geometric Dependence of Effective Properties. (a) Effective mass, stiffness, and damping ratios as a function of φ_1 for $\ell_1+\ell_2 = 0.12$ and $(x_C, y_C) = (0.02a, 0.02a)$. Stiffness and damping ratios calculated for $\ell_{B1} = \{0.8\ell_{C1}, 0.85\ell_{C1}\}$ (b) Iso-contours of effective mass ratio, m_r, for $\varphi_1 = \pi/8$ and $\bar{m}_a = 1/10$. (c) Effective stiffness ratio, k_r, for $\varphi_1 = \pi/10$ and $\bar{k}_a = 4$. Shaded region (black) in (b) and (c) denote a forbidden geometry, i.e., $\ell_1 + \ell_2 > \sqrt{x_C^2 + y_C^2}$ or $|\ell_1 - \ell_2| < \sqrt{x_C^2 + y_C^2}$.

inertial amplification effect for $s = 2$. In addition, the similar formulation $\bar{c}_{\text{eff}}$ and $\bar{k}_{\text{eff}}$ in combination with the co-location of B′ and B″ explains the tandem behavior of c_r and k_r curves. Furthermore, as illustrated by the evolution of the plots as $\bar{\ell}_{B1}$ is varied, the location of B′ acts to scale c_r and k_r. The angle at which each curve attains the maximum may be calculated from Eqs. (5). In Figs. 2b,c, the component bar lengths remain fixed while φ_s, φ_s', and φ_s'' vary in response to changing the location of node C. Unless otherwise stated, in the following, the tuning element is constructed using the above material parameters along with $(x_C, y_C) = (0.02a, 0.02a)$, $\bar{\ell}_1 + \bar{\ell}_2 = 0.12$, and $\bar{\ell}_{B1} = 0.8\bar{\ell}_{C1}$. For the mass component, $\varphi_1 = \pi/8$; for the damping and stiffness components, $\varphi_1' = \varphi_1'' = \pi/10$. Consequently, $m_{\text{eff}}^{(1)} = 6.24$, $m_{\text{eff}}^{(2)} = 1.45$, $c_{\text{eff}}^{(1)} = 1.31$, $c_{\text{eff}}^{(2)} = 0.5$, $k_{\text{eff}}^{(1)} = 3.15$, and $k_{\text{eff}}^{(2)} = 1$.

III. DYNAMIC ANALYSIS

In the following, we investigate the adjustable (linear) dynamic response of metamaterial architectures incorporating the multi-stable element. To this end, for an analytical treatment, we apply the free-wave formulation of Bloch theorem described by Hussein and Frazier[52] which accommodates temporal attenuation in wave amplitude. This section briefly describes the formulation and interpretation of results.

For the unit cell of a viscously-damped, periodic medium, $\mathbf{M}\ddot{\bar{\mathbf{u}}} + \mathbf{C}\dot{\bar{\mathbf{u}}} + \mathbf{K}\bar{\mathbf{u}} = \mathbf{f}$ represents the discretized equations of motion with $\mathbf{f}$ collecting the forces applied at the unit cell boundaries by its immediate neighbors. Due to the spatial periodicity of the wave solution, the motion of a point separated by lattice vector, $\mathbf{a}$, from a reference exhibits a phase shift, i.e., $\bar{\mathbf{u}}[\boldsymbol{\kappa}\cdot(\mathbf{x}+\mathbf{a}), \bar{t}] = \bar{\mathbf{u}}(\mathbf{x}, \bar{t})e^{i\boldsymbol{\kappa}\cdot\mathbf{a}}$ with wavevector, $\boldsymbol{\kappa}$. Consequently, one may write, $\bar{\mathbf{u}} = \mathbf{T}\bar{\mathbf{u}}_e$, equating the full set of degrees of freedom to the product of a wavevector-dependent transformation matrix, $\mathbf{T}$, and a subset of essential freedoms, $\bar{\mathbf{u}}_e$. Thus, in terms of $\bar{\mathbf{u}}_e$, the metamaterial governing equations are $\mathbf{M}_e\ddot{\bar{\mathbf{u}}}_e + \mathbf{C}_e\dot{\bar{\mathbf{u}}}_e + \mathbf{K}_e\bar{\mathbf{u}}_e = \mathbf{0}$ where $\mathbf{M}_e = \mathbf{T}^H\mathbf{M}\mathbf{T}$, $\mathbf{M}_e = \mathbf{T}^H\mathbf{M}\mathbf{T}$, and $\mathbf{M}_e = \mathbf{T}^H\mathbf{M}\mathbf{T}$ with $(\cdot)^H$ denoting the Hermitian transpose. $\mathbf{T}^H\mathbf{f} = \mathbf{0}$ maintains that boundary forces do no work.

Following the free-wave formulation, $\bar{\mathbf{u}}_e(\bar{t}) = \tilde{\mathbf{u}}_e e^{\bar{\lambda}\bar{t}}$, where $\bar{\lambda}$ is a complex frequency. Applying the time derivatives develops a quadratic eigenvalue problem in $\bar{\lambda}$. Alternatively, the governing equation can be recast in the state-space form, $\mathbf{A}\dot{\bar{\mathbf{y}}} + \mathbf{B}\bar{\mathbf{y}} = \mathbf{0}$, where

$$\mathbf{A} = \begin{bmatrix} \mathbf{0} & \mathbf{M}_e \\ \mathbf{M}_e & \mathbf{C}_e \end{bmatrix}, \quad \mathbf{B} = \begin{bmatrix} -\mathbf{M}_e & \mathbf{0} \\ \mathbf{0} & \mathbf{K}_e \end{bmatrix}, \quad \bar{\mathbf{y}} = \begin{bmatrix} \dot{\bar{\mathbf{u}}}_e \\ \bar{\mathbf{u}}_e \end{bmatrix}.$$

Assuming the solution, $\bar{\mathbf{y}}(\bar{t}) = \tilde{\mathbf{y}}e^{\bar{\eta}\bar{t}}$, formulates the standard eigenvalue problem in complex frequency, $\bar{\eta}$. The solutions appear in conjugate pairs of the form, $\bar{\eta} = -\xi\bar{\omega}_{\text{res}} \pm i\bar{\omega}_d$, where $\bar{\omega}_{\text{res}}$ is the resonant frequency, $\bar{\omega}_d = \text{Im}[\bar{\eta}]$ the damped natural frequency, and $\xi = -\text{Re}[\bar{\eta}]/\text{Abs}[\bar{\eta}]$ the damping ratio.

We complement the Bloch analysis with a simulation of a finite structure for which the nonlinear terms in the governing equations are maintained. In addition, the numerical model utilizes mechanism links of finite stiffness, $k_\ell \gg k$, which introduces additional, predominantly high-frequency modes of oscillation but, otherwise, does not affect the dynamics related to kinematic amplification[17]. However, numerical stability, then requires assigning a negligible mass, $\bar{m}_o = 10^{-3}$, to

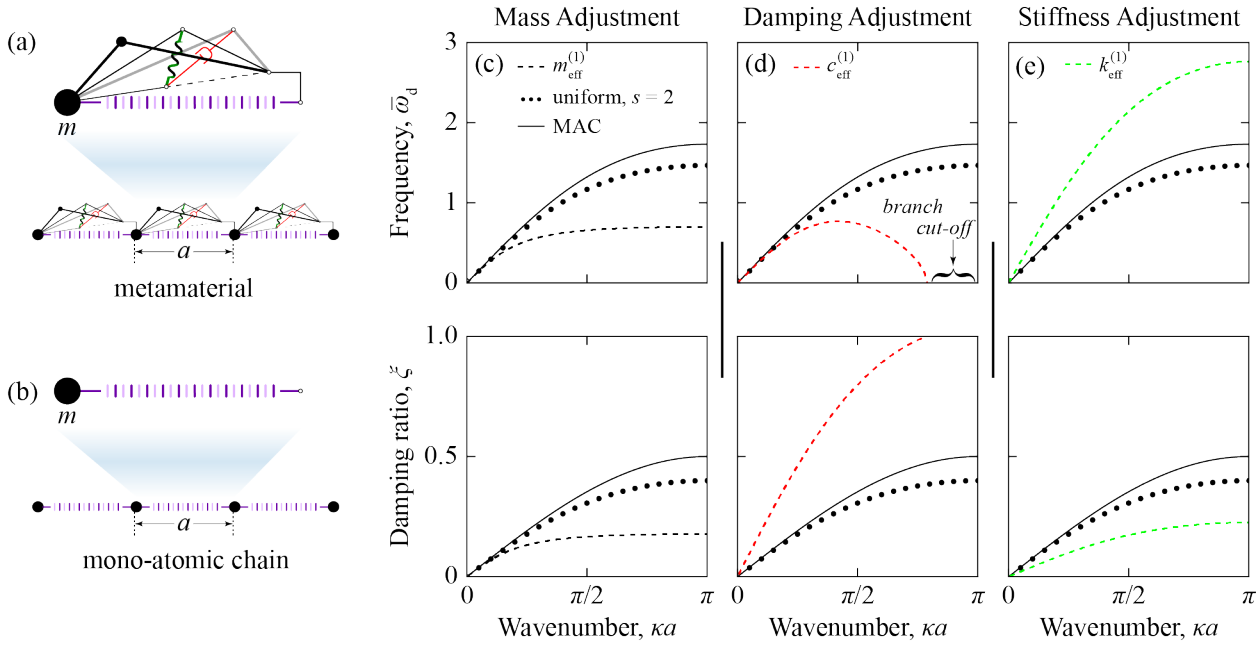

FIG. 3. Frequency Band Structure (1D). (a) 1D metamaterial with tuning element unit cell. (b) Mono-atomic chain (MAC) representing the base structure of the metamaterial, i.e., the scenario in which the kinematic amplification components are absent. (c–e) Configuration-dependent metamaterial frequency and damping ratio band structures. From tuning element components uniformly in state $s = 2$, selectively switching one component to $s = 1$ amplifies the associated effective property, yielding (c) low-frequency band gaps, (d) metadamping and branch cut-off, and (e) increased long-wavelength sound speed.

nodes A′ and A″. We utilize $k_\ell/k = 10^3$, which is well beyond what is necessary for results to converge.

IV. RESULTS AND DISCUSSION

A. 1D Metamaterial

To demonstrate the tuning ability afforded by the multi-stable element, we first consider the dispersion of the one-dimensional metamaterial in Fig. 3a for which Eq. (4) provides the matrices of the corresponding equation of motion. Following the application of Bloch theorem via $\mathbf{T}^{\mathrm{T}} = [1 \quad e^{i\kappa a}]$, the state-space determinantal equation is found to be:

$$\bar{\eta}^2(m_{\mathrm{eff}} - \delta_{12}[1+\cos(\kappa a)]\bar{m}_{\mathrm{a}}) + 4\sin^2\left(\frac{\kappa a}{2}\right)(\bar{\eta}c_{\mathrm{eff}} + k_{\mathrm{eff}}) = 0,$$

which the presence of m_{eff}, c_{eff}, and k_{eff} renders configuration-specific, an attribute extending to $\bar{\omega}_{\mathrm{d}}$ and ξ. We also consider the dynamics of the mono-atomic chain (MAC) in Fig. 3b which represents the metamaterial base structure and, therefore, lacks the amplifying components.

Figures 3c–e display the metamaterial dispersion response as each component of the tuning element is activated in turn. For clarity, of the eight possible tuning element configurations, we highlight only four: the case in which components are uniformly in state $s = 2$, therefore, minimizing the affect of kinematic amplification; and the three cases in which one component is singularly in state $s = 1$. Results for all eight configurations are available in Fig. S1c. Comparing the dispersion results of the uniform case to those of the MAC, reveals a close alignment due to the aforementioned diminution of the kinematic amplification effect, a result which is exacerbated in the long-wavelength limit ($\kappa a \to 0$) as the relative motion between nodes 1 and 2 to which the motion at A (equiv. A′, A″) is proportional becomes vanishingly small. In fact, the long-wavelength sound speed of the uniform metamaterial, $c_0 = 0.945$, is nearly identical to that of the MAC, $c_0^{\mathrm{MAC}} = 0.994$. In each case, beyond a maximum frequency, $\bar{\omega}_{\mathrm{d}}^{\max}$, and damping ratio, $\xi^{\max}$, a semi-infinite gap opens; for the metamaterial, $\bar{\omega}_{\mathrm{d}}^{\max} = 1.468$ and $\xi^{\max} = 0.4$. In Fig. 3c, switching only the effective mass component to configuration $s = 1$ brings a near four-fold increase in m_{eff}, leading to a decrease in the maximum frequency and damping ratio while the sound speed remains unaffected. Similarly, in Fig. 3d, switching only the effective damping component to configuration $s = 1$ more than doubles c_{eff}, decreasing the maximum frequency and increasing the damping ratio while maintaining the sound speed. In addition, we also observe *branch cut-off*, the condition whereby $\bar{\omega}_{\mathrm{d}} \not> 0$ over the whole Brillouin zone due to a corresponding $\xi \geq 1$ (i.e., overdamping); thus, opening gaps in the wavenumber range[52]. Moreover, the

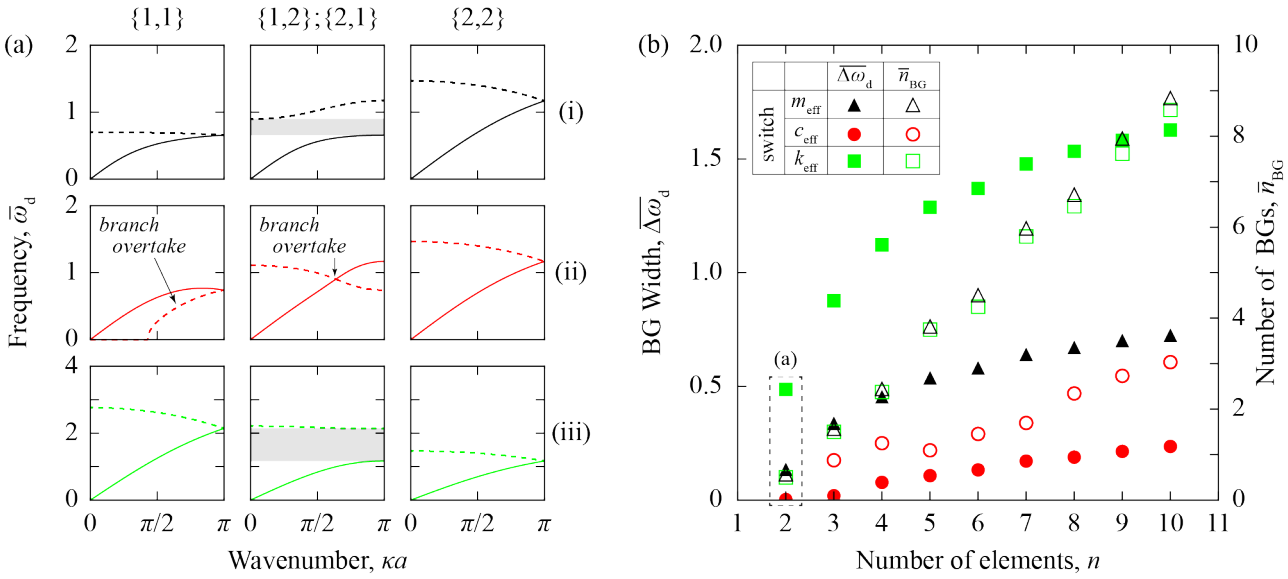

FIG. 4. Band Gap Evolution (color online). (a) The frequency diagram (band gaps shaded) depicting the acoustic (solid) and optical (dashed) branch of 1D metamaterial defined by a two-element unit cell where the configuration, {s,s}, of the constituent (i) mass, (ii) damping, or (iii) stiffness components is altered while that of the other two property components is uniformly $s = 2$. (b) The average band-gap width, $\overline{\Delta\omega}_d$ (solid), and the average number of band gaps, $\bar{n}_{BG}$ (hollow), among all (i) m_{eff} (black), (ii) c_{eff} (red), and (iii) k_{eff} (green) configurations of a n-element unit cell.

scenarios depicted in Figs. 3c,d demonstrate the concept of *metadamping*, a reduction (*negative*) or amplification (*positive*) of dissipative power between two statically equivalent configurations (i.e., identically prescribed mass, damping, effective stiffness)[53]. Similar result were also reported by Hussein *et al.*[53] and Al Ba'ba'a *et al.*[32]. In particular, Hussein *et al.*, who first demonstrated negative metadamping, analyze a system of fixed properties and combined inertial amplification and local resonance, revealing a trade-off between metadamping and spatial attenuation. Al Ba'ba'a and company demonstrated an *in situ* tunable electro-mechanical system of piezoelectric shunting circuits which exploit kinematic amplification for positive metadamping. In Fig. 3e, switching only the effective stiffness component to configuration $s = 1$ triples k_{eff}, leading to an increase in the maximum frequency and sound speed while the damping ratio decreases. The frequency and damping ratio scaling observed in Figs. 3c–e can be understood by relating the wave dispersion results at the boundary of the irreducible Brillouin zone ($\kappa a = \pi$) to the vibration of an isolated unit cell for which $\bar{\omega}_d = \sqrt{4k_{eff}(1-\xi^2)/m_{eff}}$ and $\xi = c_{eff}/\sqrt{k_{eff}m_{eff}}$.

Since each bi-stable component can be independently configured, the spatial distribution of effective properties as well as the emerging dynamic response are extremely customizable. Consider, now, a 1D metamaterial unit cell of n tuning elements which supports 2^{3n} configurations and, due to equivalent dynamics among certain configurations, a lesser number of unique dispersion responses. The n-element unit cell permits a non-uniform property distribution conducive to the formation of finite band gaps as exemplified by the results in Fig. 4a for $n = 2$. In addition, we observe *branch overtaking* – the scenario whereby damping leads to higher modes occupying a frequency range below lower ones – between the acoustic and optical modes[52]. Figure 4b tracks the average band-gap width, $\overline{\Delta\omega}_d$, and the average number of band gaps, $\bar{n}_{BG}$ for a n-element system (i) of uniform $k_{eff}^{(2)}$ and $c_{eff}^{(2)}$, and the 2^n configurations of m_{eff}, (ii) of uniform $m_{eff}^{(2)}$ and $k_{eff}^{(2)}$, and the 2^n configurations of c_{eff} and (iii) of uniform $m_{eff}^{(2)}$ and $c_{eff}^{(2)}$, and the 2^n configurations of k_{eff}. As n increases, each scenario exhibits a monotonic increase in $\overline{\Delta\omega}_d$ which, nevertheless, appears to asymptotically approach a limiting value. Further inspection of the band structures reveals that this result reflects the tendency of unit cell morphologies to broaden band gaps at higher frequencies while gaps at lower frequencies either shrink or close. Moreover, although a n-element system may exhibit up to $n-1$ band gaps, due to the band-gap closures that manifest for certain configurations, Fig. 4b shows $\bar{n}_{BG} \leq n-1$. The band gaps tend to be wider when varying the stiffness, followed by the inertial and damping induced band gaps, consistent with the nature of dependency of $\bar{\omega}_d$ on the specific properties. Compared to the variable m_{eff} and k_{eff} distribution scenarios, the case of variable c_{eff} distribution sees lower $\overline{\Delta\omega}_d$ and $\bar{n}_{BG}$ owing to annihilation of band gaps by the unique conditions branch overtaking and overdamping[52].

B. 2D Metamaterial

Figure 5a shows the unit cell of a square lattice incorporating the multi-stable element along both its horizontal and vertical edges. The corresponding matrices $\mathbf{M}$, $\mathbf{C}$, $\mathbf{K}$, and $\mathbf{T}$ are provided in the Appendix. Different from the previous example, here, $\bar{\ell}_1 + \bar{\ell}_2 = 0.4$, $\varphi_1 = \varphi_1' = \varphi_1'' = 0.03\pi$, and $\bar{\ell}_{\mathrm{B1}} = -4\bar{\ell}_{\mathrm{C1}}$, yielding effective property ratios of $m_{\mathrm{r}} = 31$ and $k_{\mathrm{r}} = 26$. Although $c_{\mathrm{r}} = 19$, compared to the previous example, the attenuation experienced by propagating waves is significantly reduced by keeping the damping small, i.e., $\bar{c} = 1/200$ and $\bar{c}_{\mathrm{a}} = 3/200$. Apparently, setting the tuning element along each axis to different configurations generates an anisotropic response in one or more of the effective properties which may assist the realization of tunable directional behavior. Nevertheless, following the procedure outlined in Sec. III, we determine the two-dimensional dispersion relations, for three cases for which $c_{\mathrm{eff}}^{(2)}$ and the tuning elements along each axis are in identical states: (i) $m_{\mathrm{eff}}^{(2)}$ and $k_{\mathrm{eff}}^{(2)}$, (ii) $m_{\mathrm{eff}}^{(2)}$ and $k_{\mathrm{eff}}^{(1)}$, and (iii) $m_{\mathrm{eff}}^{(1)}$ and $k_{\mathrm{eff}}^{(1)}$. Figure 5b reflects the dynamics of each of these unit cell configurations, the longitudinal mode (solid) exhibiting behavior reminiscent of that exhibited by the 1D system.

In order to support the analytical dispersion results as well as to demonstrate the tuning element as a mechanism for realizing functionality, we simulate the dynamic response of a 14×14 square lattice for which, of the myriad available morphologies, the particular spatial distribution of unit cell configurations and corresponding effective properties is set in the form of a waveguide (Fig. 5c). We prescribe a small-amplitude, sinusoidal displacement at the left boundary and depict the response in Figs. 5d,e. For an excitation frequency, $\bar{\omega} = 4.82$ (Fig. 5d), waves propagate along the channel defined by unit cells with tuning elements in configuration (ii) and, otherwise, decay since the excitation frequency falls within a semi-infinite band gap. Alternately, for an excitation frequency, $\bar{\omega} = 2.60$, the bulk of the wave energy is directed from the horizontal portion of channel of configuration (ii) and into that of configuration (i) (Fig. 5e). Apparently, although wave propagation is supported in the vertical portion of channel (ii), since waves are no longer barred from entering channel (i), little wave energy is re-directed into the vertical column. The waveguide is just one functionality realizable post-fabrication in lattices leveraging the tuning element for effective property re-distribution.

V. CONCLUSION

In this article, we present a novel structural element which leverages geometric multi-stability and kinematic amplification to independently adjust its effective mass, stiffness, and viscous damping properties with consequences for the dynamic response of metamaterials for which it is a part of the unit cell design. This is significant since, despite the well-established impact of all three properties in mechanical vibration and wave propagation, alternative approaches typically manipulate a single parameter. In addition, the specific implementation of multi-stability in the proposed structural element ensures that re-configuration does not entail a change in length and, therefore, does not necessitate a change in the size/shape of the realized metamaterial structure, a beneficial quality in practical settings where the metamaterial structure is subject to geometric constraints.

To demonstrate the tuning ability granted by the multi-stable element, we analytically and numerically investigate the adjustable dynamic characteristics of 1D/2D metamaterial models for which it appears as a part of the unit cell. It is shown that the band structure depends on the specific configurations of the multi-stable element: the sound speed, the frequency range(s) of propagation, and the propagation modality (e.g., underdamped or overdamped) are each amenable to manipulation. Moreover, in organizing the spatial distribution of the element states, custom and re-definable mesoscopic morphologies of the effective properties are attainable with the potential for functionalization (e.g., the impromptu formation of a waveguide).

The proposed concept offers a new way to expand the performance space of lattice metamaterials post-fabrication. In addition, as a product of geometry rather than, e.g., specific material constituents or external apparatuses, the proposed technique promises a flexible implementation, and is amenable to current and emerging additive manufacturing technologies.

APPENDIX

Kinematic Relations

In addition to the tuning ability provided by the multi-stable element, the effective properties enabled by the amplified motion of each two-bar linkage is central to the metamaterial performance. For the inclined, two-bar linkage components utilized in this article, Frazier[51] derives relations for the amplified displacement at node A (equivalently, A′ and A″) in terms of the displacements at nodes 1 and 2. To arrive at these relations, consider the length of each rigid link of the component: $\ell_1^2 = (x_{\mathrm{A}} - x_1)^2 + (y_{\mathrm{A}} - y_1)^2$ and $\ell_2^2 = (x_{\mathrm{A}} - x_{\mathrm{C}})^2 + (y_{\mathrm{A}} - y_{\mathrm{C}})^2$. The corresponding differentials are given by:

$$(x_{\mathrm{A}} - x_1)(\bar{u}_{\mathrm{A}} - \bar{u}_1) + (y_{\mathrm{A}} - y_1)(\bar{v}_{\mathrm{A}} - \bar{v}_1) = 0, \quad \text{(A1a)}$$

$$(x_{\mathrm{A}} - x_{\mathrm{C}})(\bar{u}_{\mathrm{A}} - \bar{u}_2) + (y_{\mathrm{A}} - y_{\mathrm{C}})(\bar{v}_{\mathrm{A}} - \bar{v}_2) = 0, \quad \text{(A1b)}$$

where $\delta x_{\mathrm{A}} \to \bar{u}_{\mathrm{A}}$, $\delta y_{\mathrm{A}} \to \bar{v}_{\mathrm{A}}$, $\delta x_{\mathrm{C}} \to \bar{u}_2$, $\delta y_{\mathrm{C}} \to \bar{v}_2$, and $\delta x_1 \to \bar{u}_1$. Simultaneously solving Eqs. (A1) yields the

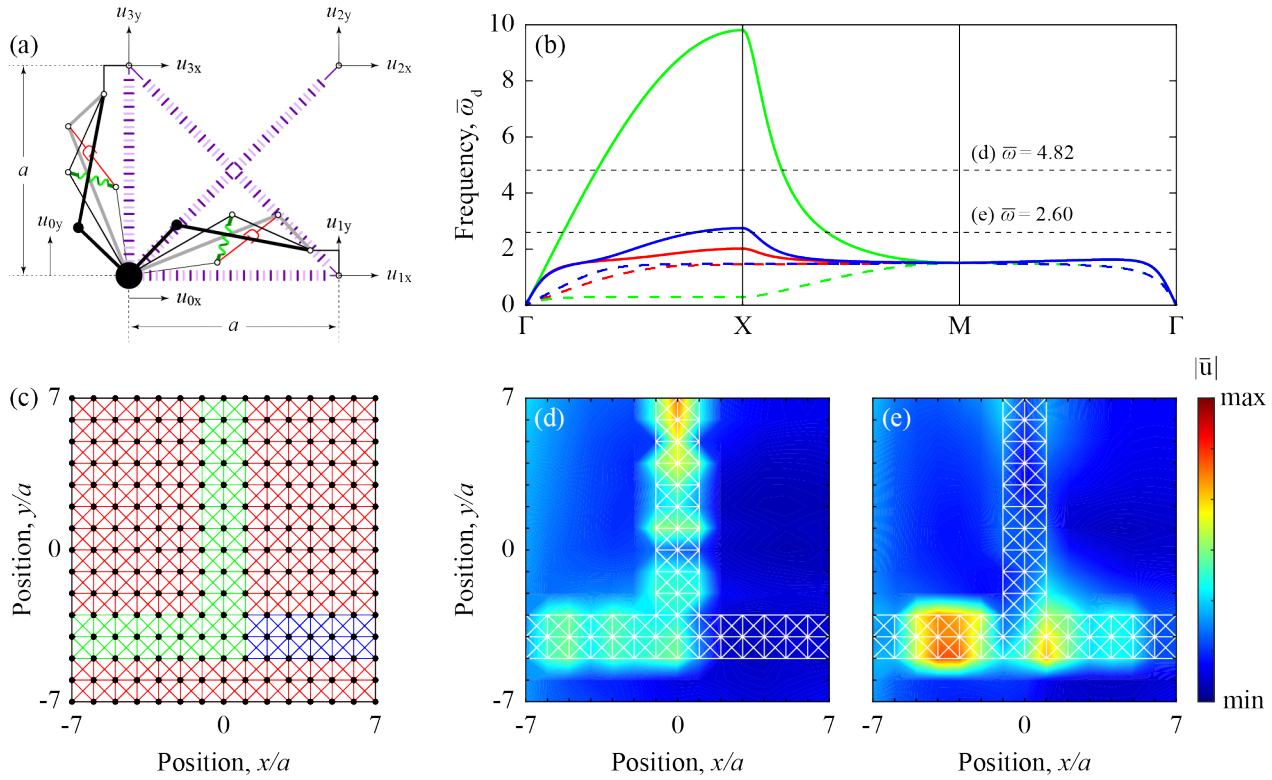

FIG. 5. Customizable Waveguide (color online). (a) The 2D metamaterial unit cell with nearest- and next-nearest neighbor connections, and a tuning element oriented along both the horizontal and vertical axis. (b) Homogeneous dispersion curves [*sans* $\xi(\boldsymbol{\kappa})$] for three tuning element configurations with constant $c^{(2)}_{\text{eff}}$: (i) $m^{(2)}_{\text{eff}}$ and $k^{(2)}_{\text{eff}}$ (blue), (ii) $m^{(2)}_{\text{eff}}$ and $k^{(1)}_{\text{eff}}$ (green), and (iii) $m^{(1)}_{\text{eff}}$ and $k^{(1)}_{\text{eff}}$ (red). (c) System of 14×14 unit cells with tuning elements configured to establish a waveguide in the non-uniform distribution of effective properties. In simulation, a sinusoidal displacement, $\bar{u}_x = (5 \times 10^{-5}) \sin(\bar{\omega}\bar{t})$ for $\bar{t} \in [0, 50]$, is prescribed at the left boundary with frequency (d) $\bar{\omega} = 4.82$ and (e) $\bar{\omega} = 2.60$. Subfigures (d,e) plot the observed maximum magnitude of the displacement, $|\bar{\mathbf{u}}|$.

desired relations:

$$\bar{u}_{\text{A}} = \frac{\bar{u}_2 + \tan(\theta_s)\cot(\varphi_s)\bar{u}_1 + (\bar{v}_1 - \bar{v}_2)\tan(\theta_s)}{1 + \tan(\theta_s)\cot(\varphi_s)}, \quad \text{(A2a)}$$

$$\bar{v}_{\text{A}} = \frac{(\bar{u}_1 - \bar{u}_2)\cot(\varphi_s) + \bar{v}_1 + \bar{v}_2\tan(\theta_s)\cot(\varphi_s)}{1 + \tan(\theta_s)\cot(\varphi_s)}. \quad \text{(A2b)}$$

For the one-dimensional system, $\bar{v}_1$ and $\bar{v}_2$ vanish, reducing Eqs. (A2) to Eqs. (2):

$$\bar{u}_{\text{A}} = \frac{\bar{u}_2 + \tan(\theta_s)\cot(\varphi_s)\bar{u}_1}{1 + \tan(\theta_s)\cot(\varphi_s)},$$

$$\bar{v}_{\text{A}} = (\bar{u}_1 - \bar{u}_2)\frac{\cos(\varphi_s)\cos(\theta_s)}{\sin(\varphi_s + \theta_s)}.$$

For the motion of A′ and A″, φ_s and θ_s are simply replaced by their primed and double-primed counterparts, respectively.

For the linkage component containing m_{a}, Eqs. (A2) and Eqs. (2) are sufficient for calculating the contribution to the kinetic energy in terms of $\bar{u}_1$ and $\bar{u}_2$. In order to calculate the contribution of k_{a} and c_{a}, respectively, to the deformation energy and rate of energy loss, it is necessary to also know the motion of node B′. Given, $\bar{\ell}^2_{\text{AB}} = (x_{\text{A}} - x_{\text{B}})^2 + (y_{\text{A}} - y_{\text{B}})^2$, the length of the segment joining nodes A′ and B′, the differential gives:

$$\delta\bar{\ell}_{\text{AB}} = \cos(\alpha_s)(\bar{u}_{\text{A}} - \bar{u}_1) + \sin(\alpha_s)(\bar{v}_{\text{A}} - \bar{v}_1), \quad \text{(A4)}$$

where $\delta x_{\text{B}} \to \bar{u}_1$ and $\delta y_{\text{B}} \to \bar{v}_1$. Upon substituting the relations in Eq. (2) into Eq. (A4), we show $\delta\ell_{\text{AB}}$ to be a function of the boundary displacements, u_1 and u_2:

$$\delta\bar{\ell}_{\text{AB}} = -[u_1 - u_2 - (v_1 - v_2)\tan(\theta'_s)] \times \frac{\cos(\alpha'_s) - \sin(\alpha'_s)\cot(\varphi'_s)}{1 + \cot(\varphi'_s)\tan(\theta'_s)}, \quad \text{(A5)}$$

For the one-dimensional system where $\bar{v}_1$ and $\bar{v}_2$ vanish, reducing Eq. (A5) to the following:

$$\delta\bar{\ell}_{\text{AB}} = -\frac{(\bar{u}_1 - \bar{u}_2)[\cos(\alpha'_s) - \sin(\alpha'_s)\cot(\varphi'_s)]}{1 + \cot(\varphi'_s)\tan(\theta'_s)}. \quad \text{(A6)}$$

Square Lattice Matrix Equations

Equation (3) in the main article defines the kinetic energy, deformation energy, and rate of energy loss for a one-dimensional system comprising the multi-stable tuning element and a boundary mass. Application of the dissipative Euler-Lagrange equation generates the corresponding matrix equations of motion. Here, the procedure is repeated for a two-dimensional system and, ultimately, is utilized to develop the matrix definitions for the square lattice unit cell of Sec. IV B.

Isolated, the energetics of the tuning element are given by $T = \frac{1}{2}\bar{m}_{\rm a}\dot{\bar{u}}_{\rm A}^2 + \frac{1}{2}\bar{m}_{\rm a}\dot{\bar{v}}_{\rm A}^2$, $V = \frac{1}{2}\bar{k}_{\rm a}(\delta\bar{\ell}_{\rm AB})^2$, and $R = \frac{1}{2}\bar{c}_{\rm a}(\delta\dot{\bar{\ell}}_{\rm AB})^2$. Upon substitution of Eqs. (A2) and (A5) into T, V, and R, the configuration-specific $\mathbf{M}_{\rm a}$, $\mathbf{C}_{\rm a}$, and $\mathbf{K}_{\rm a}$ are derived as follows:

$$\mathbf{M}_{\rm a} = \partial_t(\partial_{\dot{\mathbf{u}}}T) = \bar{m}_{\rm a}\begin{bmatrix}\delta_{11} & \delta_{12} & -\delta_{13} & \delta_{14}\\ & \delta_{22} & -\delta_{23} & \delta_{24}\\ & \text{symm.} & \delta_{33} & -\delta_{34}\\ & & & \delta_{44}\end{bmatrix},$$

$$\mathbf{C}_{\rm a} = \partial_{\dot{\mathbf{u}}}R = \bar{c}_{\rm a}\varepsilon_{\rm c}\begin{bmatrix}1 & -\gamma & -1 & \gamma\\ & \gamma^2 & \gamma & -\gamma^2\\ & \text{symm.} & 1 & -\gamma\\ & & & \gamma^2\end{bmatrix},$$

$$\mathbf{K}_{\rm a} = \partial_{\dot{\mathbf{u}}}V = \bar{k}_{\rm a}\varepsilon_{\rm k}\begin{bmatrix}1 & -\mu & -1 & \mu\\ & \mu^2 & \mu & -\mu^2\\ & \text{symm.} & 1 & -\mu\\ & & & \mu^2\end{bmatrix},$$

written consistent with $\mathbf{u}^{\rm T} = [\mathbf{u}_1 \quad \mathbf{u}_2]$, where $\mathbf{u}_i^{\rm T} = [u_i \;\; v_i]$ and $i = 1, 2$ is the node number. In the preceding,

$$\begin{aligned}
\delta_{11} &= [\cos(\varphi_s)\csc(\varphi_s+\theta_s)]^2,\\
\delta_{12} &= \delta_{21} = \cos(\varphi_s)\sin(\varphi_s)\csc(\varphi_s+\theta_s)^2,\\
\delta_{13} &= \delta_{31} = \cos(\varphi_s)\cos(\theta_s)\cot(\varphi_s+\theta_s)\csc(\varphi_s+\theta_s),\\
\delta_{14} &= \delta_{41} = \cos(\varphi_s)\sin(\theta_s)\cot(\varphi_s+\theta_s)\csc(\varphi_s+\theta_s),\\
\delta_{22} &= [\sin(\varphi_s)\csc(\varphi_s+\theta_s)]^2,\\
\delta_{23} &= \delta_{32} = \sin(\varphi_s)\cos(\theta_s)\cot(\varphi_s+\theta_s)\csc(\varphi_s+\theta_s),\\
\delta_{24} &= \delta_{42} = \sin(\varphi_s)\sin(\theta_s)\cot(\varphi_s+\theta_s)\csc(\varphi_s+\theta_s),\\
\delta_{33} &= [\cos(\theta_s)\csc(\varphi_s+\theta_s)]^2,\\
\delta_{34} &= \delta_{43} = \cos(\theta_s)\sin(\theta_s)\csc(\varphi_s+\theta_s)^2,\\
\delta_{44} &= [\sin(\theta_s)\csc(\varphi_s+\theta_s)]^2\\
\mu &= \tan(\theta_s'),\\
\gamma &= \tan(\theta_s'').
\end{aligned}$$

Following an assembly process, $\mathbf{M}_{\rm a}$, $\mathbf{C}_{\rm a}$, and $\mathbf{K}_{\rm a}$ are incorporated into the system matrices, $\mathbf{M}$, $\mathbf{C}$, and $\mathbf{K}$ of the particular two-dimensional system. For the square lattice considered in the main, these matrices for the unit cell are given by:

$$\mathbf{M} = \bar{m}_{\rm a}\begin{bmatrix}
1/\bar{m}_{\rm a}+\delta_{11}^{\rm h}+\delta_{22}^{\rm v} & \delta_{12}^{\rm h}-\delta_{12}^{\rm v} & -\delta_{13}^{\rm h} & \delta_{14}^{\rm h} & 0 & 0 & \delta_{24}^{\rm v} & \delta_{23}^{\rm v}\\
& 1/\bar{m}_{\rm a}+\delta_{22}^{\rm h}+\delta_{11}^{\rm v} & -\delta_{23}^{\rm h} & \delta_{24}^{\rm h} & 0 & 0 & -\delta_{14}^{\rm v} & -\delta_{13}^{\rm v}\\
& & \delta_{33}^{\rm h} & -\delta_{34}^{\rm h} & 0 & 0 & 0 & 0\\
& & & \delta_{44}^{\rm h} & 0 & 0 & 0 & 0\\
& & & & 0 & 0 & 0 & 0\\
& & \text{symm.} & & & 0 & 0 & 0\\
& & & & & & \delta_{44}^{\rm v} & \delta_{34}^{\rm v}\\
& & & & & & & \delta_{33}^{\rm v}
\end{bmatrix},$$

$$\mathbf{C} = \frac{1}{2}\begin{bmatrix}
3\bar{c}+2\bar{c}_{\rm a}\varepsilon_{\rm c}[1+(\gamma^{\rm v})^2] & \bar{c}-2\bar{c}_{\rm a}\varepsilon_{\rm c}(\gamma^{\rm h}-\gamma^{\rm v}) & -2(\bar{c}+\bar{c}_{\rm a}\varepsilon_{\rm c}) & 2\bar{c}_{\rm a}\varepsilon_{\rm c}\gamma^{\rm h} & -\bar{c} & -\bar{c} & -2\bar{c}_{\rm a}\varepsilon_{\rm c}(\gamma^{\rm v})^2 & -2\bar{c}_{\rm a}\varepsilon_{\rm c}\gamma^{\rm v}\\
& 3\bar{c}+2\bar{c}_{\rm a}\varepsilon_{\rm c}[1+(\gamma^{\rm h})^2] & 2\bar{c}_{\rm a}\varepsilon_{\rm c}\gamma^{\rm h} & -2\bar{c}_{\rm a}\varepsilon_{\rm c}(\gamma^{\rm h})^2 & -\bar{c} & -\bar{c} & -2\bar{c}_{\rm a}\varepsilon_{\rm c}\gamma^{\rm v} & -2(\bar{c}+\bar{c}_{\rm a}\varepsilon_{\rm c})\\
& & 3\bar{c}+2\bar{c}_{\rm a}\varepsilon_{\rm c} & -(\bar{c}+2\bar{c}_{\rm a}\varepsilon_{\rm c}\gamma^{\rm h}) & 0 & 0 & -\bar{c} & \bar{c}\\
& & & \bar{c}+2\bar{c}_{\rm a}\varepsilon_{\rm c}(\gamma^{\rm h})^2 & 0 & 0 & \bar{c} & -\bar{c}\\
& & & & \bar{c} & \bar{c} & 0 & 0\\
& & \text{symm.} & & & \bar{c} & 0 & 0\\
& & & & & & \bar{c}+2\bar{c}_{\rm a}\varepsilon_{\rm c}(\gamma^{\rm v})^2 & -\bar{c}+2\bar{c}_{\rm a}\varepsilon_{\rm c}\gamma^{\rm v}\\
& & & & & & & 3\bar{c}+2\bar{c}_{\rm a}\varepsilon_{\rm c}
\end{bmatrix},$$

$$\mathbf{K} = \frac{1}{2}\begin{bmatrix}
3+2\bar{k}_{\rm a}\varepsilon_{\rm k}[1+(\mu^{\rm v})^2] & 1-2\bar{k}_{\rm a}\varepsilon_{\rm k}(\mu^{\rm h}-\mu^{\rm v}) & -2(1+\bar{k}_{\rm a}\varepsilon_{\rm k}) & 2\bar{k}_{\rm a}\varepsilon_{\rm k}\mu^{\rm h} & -1 & -1 & -2\bar{k}_{\rm a}\varepsilon_{\rm k}(\mu^{\rm v})^2 & -2\bar{k}_{\rm a}\varepsilon_{\rm k}\mu^{\rm v}\\
& 3+2\bar{k}_{\rm a}\varepsilon_{\rm k}[1+(\mu^{\rm h})^2] & 2\bar{k}_{\rm a}\varepsilon_{\rm k}\mu^{\rm h} & -2\bar{k}_{\rm a}\varepsilon_{\rm k}(\mu^{\rm h})^2 & -1 & -1 & -2\bar{k}_{\rm a}\varepsilon_{\rm k}\mu^{\rm v} & -2(1+\bar{k}_{\rm a}\varepsilon_{\rm k})\\
& & 3+2\bar{k}_{\rm a}\varepsilon_{\rm k} & -(1+2\bar{k}_{\rm a}\varepsilon_{\rm k}\mu^{\rm h}) & 0 & 0 & -1 & 1\\
& & & 1+2\bar{k}_{\rm a}\varepsilon_{\rm k}(\mu^{\rm h})^2 & 0 & 0 & 1 & -1\\
& & & & 1 & 1 & 0 & 0\\
& & \text{symm.} & & & 1 & 0 & 0\\
& & & & & & 1+2\bar{k}_{\rm a}\varepsilon_{\rm k}(\mu^{\rm v})^2 & -1+2\bar{k}_{\rm a}\varepsilon_{\rm k}\mu^{\rm v}\\
& & & & & & & 3+2\bar{k}_{\rm a}\varepsilon_{\rm k}
\end{bmatrix},$$

consistent with $\bar{\mathbf{u}}^{\mathrm{T}} = [\bar{\mathbf{u}}_0 \;\; \bar{\mathbf{u}}_1 \;\; \bar{\mathbf{u}}_2 \;\; \bar{\mathbf{u}}_3]$. Coefficients, $(\cdot)^{\mathrm{h}}$ and $(\cdot)^{\mathrm{v}}$, pertain to the bi-stable components along the horizontal and vertical edges of the unit cell, respectively. For $\mathbf{u}_{\mathrm{e}}^{\mathrm{T}} = [u_0 \;\; v_0]$, the corresponding Bloch transformation matrix is given by:

$$\mathbf{T} = \begin{bmatrix} 1 & 0 \\ 0 & 1 \\ p_{\mathrm{x}} & 0 \\ 0 & p_{\mathrm{x}} \\ p_{\mathrm{x}}p_{\mathrm{y}} & 0 \\ 0 & p_{\mathrm{x}}p_{\mathrm{y}} \\ p_{\mathrm{y}} & 0 \\ 0 & p_{\mathrm{y}} \end{bmatrix}$$

where $p_{\mathrm{x}} = \mathrm{e}^{\mathrm{i}\kappa_{\mathrm{x}}a}$ and $p_{\mathrm{y}} = \mathrm{e}^{\mathrm{i}\kappa_{\mathrm{y}}a}$.

[1] T. Han, X. Bai, D. Gao, J. T. Thong, B. Li, and C.-W. Qiu, "Experimental demonstration of a bilayer thermal cloak," *Phys. Rev. Lett.*, vol. 112, p. 054302, March 2014.

[2] L. Xu, S. Yang, and J. Huang, "Passive metashells with adaptive thermal conductivities: chameleonlike behavior and its origin," *Phys. Rev. Appl.*, vol. 11, p. 054071, May 2019.

[3] F. Zangeneh-Nejad and R. Fleury, "Topological analog signal processing," *Nat. Commun.*, vol. 10, p. 2058, May 2019.

[4] F. L. Jiménez, P. Upadhyaya, J. Liljenhjerte, P. M. Reis, and S. Kumar, "Soft optical composites for tunable transmittance," *Extreme Mech. Lett.*, vol. 9, pp. 297–303, 2016.

[5] O. R. Bilal, D. Ballagi, and C. Daraio, "Architected lattices for simultaneous broadband attenuation of airborne sound and mechanical vibrations in all directions," *Phys. Rev. Appl.*, vol. 10, no. 5, p. 054060, 2018.

[6] Z. Xiao, P. Gao, D. Wang, X. He, and L. Wu, "Ventilated metamaterials for broadband sound insulation and tunable transmission at low frequency," *Extreme Mech. Lett.*, vol. 46, p. 101348, 2021.

[7] A. Palermo, Y. Wang, P. Celli, and C. Daraio, "Tuning of surface-acoustic-wave dispersion via magnetically modulated contact resonances," *Phys. Rev. Appl.*, vol. 11, no. 4, p. 044057, 2019.

[8] H. Yang and L. Ma, "Multi-stable mechanical metamaterials with shape-reconfiguration and zero Poisson's ratio," *Mater. Des.*, vol. 152, pp. 181–190, August 2018.

[9] S. Mhatre, E. Boatti, D. Melancon, A. Zareei, M. Dupont, M. Bechthold, and K. Bertoldi, "Deployable structures based on buckling of curved beams upon a rotational input," *Adv. Funct. Mater.*, vol. 31, no. 35, p. 2101144, 2021.

[10] J. E. Pechac and M. J. Frazier, "Metamaterial design strategy for mechanical energy absorption under general loading," *Extreme Mech. Lett.*, vol. 51, p. 101580, 2022.

[11] S. G. Higgins, M. Becce, A. Belessiotis-Richards, H. Seong, J. E. Sero, and M. M. Stevens, "High-aspect-ratio nanostructured surfaces as biological metamaterials," *Adv. Mater.*, vol. 32, no. 9, p. 1903862, 2020.

[12] Y. Roh, S.-H. Lee, J. Kwak, H. S. Song, S. Shin, Y. K. Kim, J. W. Wu, B.-K. Ju, B. Kang, and M. Seo, "Terahertz imaging with metamaterials for biological applications," *Sens. Actuators B Chem.*, vol. 352, p. 130993, 2022.

[13] M. I. Hussein, M. J. Leamy, and M. Ruzzene, "Dynamics of phononic materials and structures: historical origins, recent progress, and future outlook," *Appl. Mech. Rev.*, vol. 66, p. 040802, May 2014.

[14] Z. Yang, J. Mei, M. Yang, N. H. Chan, and P. Sheng, "Membrane-type acoustic metamaterial with negative dynamic mass," *Phys. Rev. Lett.*, vol. 101, p. 204301, November 2008.

[15] N. X. Fang, D. Xi, J. Xu, M. Ambati, W. Srituravanich, C. Sun, and X. Zhang, "Ultrasonic metamaterials with negative modulus," *Nat. Mater.*, vol. 5, pp. 452–456, June 2006.

[16] M. Farhat, S. Guenneau, S. Enoch, A. B. Movchan, and G. G. Petursson, "Focussing bending waves via negative refraction in perforated thin plates," *Appl. Phys. Lett.*, vol. 96, p. 081909, February 2010.

[17] C. Yilmaz, G. M. Hulbert, and N. Kikuchi, "Phononic band gaps induced by inertial amplification in periodic media," *Phys. Rev. B*, vol. 76, p. 054309, August 2007.

[18] M. I. Hussein and M. J. Frazier, "Metadamping: An emergent phenomenon in dissipative metamaterials," *J. Sound Vib.*, vol. 332, pp. 4767–4774, September 2013.

[19] S. Yang, J. H. Page, Z. Liu, M. L. Cowan, C. T. Chan, and P. Sheng, "Ultrasound Tunneling through 3D Phononic Crystals," *Physical Review Letters*, vol. 88, p. 104301, February 2002.

[20] R. Süsstrunk and S. D. Huber, "Observation of phononic helical edge states in a mechanical topological insulator," *Science*, vol. 349, pp. 47–50, July 2015.

[21] H. Xue, Y. Yang, F. Gao, Y. Chong, and B. Zhang, "Acoustic higher-order topological insulator on a kagome lattice," *Nat. Mater.*, vol. 18, pp. 108–112, February 2019.

[22] M. Miniaci and R. K. Pal, "Design of topological elastic waveguides," *J. Appl. Phys.*, vol. 130, p. 141101, October 2021.

[23] I. Antoniadis, D. Chronopoulos, V. Spitas, and D. Koulocheris, "Hyper-damping properties of a stiff and stable linear oscillator with a negative stiffness element," *J. Sound Vib.*, vol. 346, pp. 37–52, 2015.

[24] J. Mei, G. Ma, M. Yang, Z. Yang, W. Wen, and P. Sheng, "Dark acoustic metamaterials as super absorbers for low-frequency sound," *Nat. Commun.*, vol. 3, no. 1, pp. 1–7, 2012.

[25] C. Daraio, V. F. Nesterenko, E. B. Herbold, and S. Jin, "Tunability of solitary wave properties in one-dimensional strongly nonlinear phononic crystals," *Phys. Rev. E*, vol. 73, p. 026610, February 2006.

[26] R. K. Pal, J. Rimoli, and M. Ruzzene, "Effect of large deformation pre-loads on the wave properties of hexagonal lattices," *Smart Mater. Struct.*, vol. 25, p. 054010, May 2016.

[27] H. Dong and Y. Hu, "Harnessing fluid pre-pressure to tune the properties of phononic crystals," *Extreme Mech. Lett.*, vol. 34, p. 100582, January 2020.

[28] B.-J. Kwon, J.-Y. Jung, D. Lee, K.-C. Park, and I.-K. Oh, "Tunable acoustic waveguide based on vibro-acoustic metamaterials with shunted piezoelectric unit cells," *Smart Mater. Struct.*, vol. 24, p. 105018, October 2015.

[29] P. Celli and S. Gonella, "Tunable directivity in metamaterials with reconfigurable cell symmetry," *Appl. Phys. Lett.*, vol. 106, p. 091905, March 2015.

[30] F. Li, C. Zhang, and C. Liu, "Active tuning of vibration and wave propagation in elastic beams with periodically placed piezoelectric actuator/sensor pairs," *J. Sound Vib.*, vol. 393, pp. 14–29, April 2017.

[31] G. Wang, J. Cheng, J. Chen, and Y. He, "Multi-resonant piezoelectric shunting induced by digital controllers for subwavelength elastic wave attenuation in smart metamaterial," *Smart Mater. Struct.*, vol. 26, p. 025031, February 2017.

[32] H. Al Ba'ba'a, Z. Lin, and S. Tol, "Metadamping enhancement and tunability via scissor-like electromechanical metamaterials," *J. Appl. Phys.*, vol. 130, no. 18, p. 184901, 2021.

[33] A. Darabi, E. Kliewer, and M. J. Leamy, "Reconfigurable acoustic multiplexer/demultiplexer using time division," *Appl. Phys. Lett.*, vol. 119, p. 113501, September 2021.

[34] T. Yang, Z.-G. Song, E. Clerkin, Y.-W. Zhang, J.-H. Sun, Y.-S. Su, L.-Q. Chen, and P. Hagedorn, "A programmable nonlinear acoustic metamaterial," *AIP Adv.*, vol. 7, no. 9, p. 095323, 2017.

[35] S. Liu, Y. Zhao, D. Zhao, J. Wu, and C. Gao, "Tunable elastic wave bandgaps and waveguides by acoustic metamaterials with magnetorheological elastomer," *Acoust. Phys.*, vol. 66, pp. 123–131, March 2020.

[36] A. S. Gliozzi, M. Miniaci, A. Chiappone, A. Bergamini, B. Morin, and E. Descrovi, "Tunable photo-responsive elastic metamaterials," *Nat. Commun.*, vol. 11, May 2020.

[37]X. Ge, H. Xiang, Y. Liu, J. Shen, Y. Li, and Y. Li, "Utilizing reversible solid-liquid phase transition to tune phononic bandgaps," *AIP Adv.*, vol. 11, p. 125323, December 2021.

[38]P. Celli and S. Gonella, "Manipulating waves with LEGO (R) bricks: A versatile experimental platform for metamaterial architectures," *Appl. Phys. Lett.*, vol. 107, p. 081901, August 2015.

[39]Q. Zhang, K. Zhang, and G. Hu, "Tunable fluid-solid metamaterials for manipulation of elastic wave propagation in broad frequency range," *Appl. Phys. Lett.*, vol. 112, p. 221906, June 2018.

[40]Q. Zhang, Y. Chen, K. Zhang, and G. Hu, "Programmable elastic valley Hall insulator with tunable interface propagation routes," *Extreme Mech. Lett.*, vol. 28, pp. 76–80, April 2019.

[41]K. Bertoldi and M. C. Boyce, "Mechanically triggered transformations of phononic band gaps in periodic elastomeric structures," *Phys. Rev. B*, vol. 77, p. 052105, February 2008.

[42]C. R. Tipton, E. Han, and T. Mullin, "Magneto-elastic buckling of a soft cellular solid," *Soft Matter*, vol. 8, pp. 6880–6883, June 2012.

[43]P. Wang, F. Casadei, S. Shan, J. C. Weaver, and K. Bertoldi, "Harnessing buckling to design tunable locally resonant acoustic metamaterials," *Phys. Rev. Lett.*, vol. 113, p. 014301, July 2014.

[44]S. Rudykh and M. C. Boyce, "Transforming wave propagation in layered media via instability-induced interfacial wrinkling," *Phys. Rev. Lett.*, vol. 112, p. 034301, Jan 2014.

[45]M. D. Schaeffer and M. Ruzzene, "Wave propagation in multistable magneto-elastic lattices," *Int. J. Solids Struct.*, vol. 56–57, pp. 78–95, March 2015.

[46]M. J. Frazier and D. M. Kochmann, "Band gap transmission in periodic bistable mechanical systems," *J. Sound Vib.*, vol. 388, pp. 315–326, February 2017.

[47]J. Meaud and K. Che, "Tuning elastic wave propagation in multistable architected materials," *Int. J. Solids Struct.*, vol. 122–123, pp. 69–80, September 2017.

[48]J. Meaud, "Multistable two-dimensional spring-mass lattices with tunable band gaps and wave directionality," *J. Sound Vib.*, vol. 434, pp. 44–62, November 2018.

[49]Z. Wu, Y. Zheng, and K. W. Wang, "Metastable modular metastructures for on-demand reconfiguration of band structures and nonreciprocal wave propagation," *Phys. Rev. E*, vol. 97, p. 022209, February 2018.

[50]V. Ramakrishnan and M. J. Frazier, "Multistable metamaterial on elastic foundation enables tunable morphology for elastic wave control," *J. Appl. Phys.*, vol. 127, p. 225104, June 2020.

[51]M. J. Frazier, "Multi-stable acoustic metamaterials with re-configurable mass distribution," *J. Appl. Phys.*, 2022 (to appear).

[52]M. I. Hussein and M. J. Frazier, "Band structure of phononic crystals with general damping," *J. Appl. Phys.*, vol. 108, p. 093506, November 2010.

[53]M. I. Hussein, I. Patrick, A. Banerjee, and S. Adhikari, "Metadamping in inertially amplified metamaterials: trade-off between spatial attenuation and temporal attenuation," *submitted*, December 2021.